SI APPENDIX

Kingsley and Eliason et al. "Identity and novelty in the avian syrinx"

Methods S1: Methods for the computational fluid dynamics model investigated (Fig. 3a)

Overview

We simulated flow patterns during avian respiration using computational fluid dynamics (CFD) software (Fig. 3a) (Star-CCM+, Siemens PLM Software, Plano, Texas). We used a simplified parametric geometry to facilitate the survey of a wide range of morphologies of different avian species as depicted in Fig. S1-1.

Computational Approach

The CFD analysis was based on mesh-based discretization of the geometric model and solutions to the linearized Navier-Stokes and mass continuity equations (Eqns. S1-1 and S1-2) to yield predictions of flow velocity and pressure throughout the domain:

$$\rho\left[\frac{\partial\vec{V}}{\partial t}+\left(\vec{V}\cdot\vec{\nabla}\right)\vec{V}\right]=-\vec{\nabla}p+\mu\nabla^2\vec{V}+S \qquad \text{(S1-1)}$$

$$\frac{\partial\rho}{\partial t}+\left(\vec{\nabla}\cdot\rho\vec{V}\right)=0 \qquad \text{(S1-2)}$$

In Eqns. S2-1 and S2-2, $\vec{V}$ is the three-dimensional velocity vector, p is pressure, ρ and μ are density and viscosity, respectively, and S is any other source term, such as gravity. In these simulations the influence of gravity was considered to be negligible, thus S was zero.

The tracheal and bronchial walls were rigid. A time-varying velocity boundary condition, $V=f(t)$ corresponding to a specified breathing waveform (discussed further below) was prescribed at the surfaces at the ends of the bronchial segments. A zero-pressure boundary condition, P_0, was applied to the end of the tracheal segment. An initial condition of zero velocity everywhere was applied. The flow was laminar, unsteady, viscous, and three-dimensional. An implicit, unsteady solver was used with velocity and pressure relaxation values of 0.8 and 0.2, respectively. Each time step was considered to be converged after momentum and continuity residuals reached levels below 1×10^{-2} The fluid was modeled as incompressible air with a density of 1.184 kg/m^3 and a dynamic viscosity of 1.855×10^{-5} Pa•s. The simulation was allowed to run for two breathing cycles.

Breathing Waveform

The biomimetic time-varying pressure boundary condition at the tracheal inlets simulated continuous breathing based on a decomposition of lung pressure of an adult male zebra finch at rest, taken from data collected for the investigation by Franz and Goller (1). Procedures for that study were approved by the University of Utah IACUC protocols. We ensemble averaged several periods of the lung pressure signal and then approximated the resulting waveform using the first seven terms of a Fourier transform as shown in Fig. S1-2. Simulations run using a pressure boundary condition revealed that the resulting average velocity in the trachea matched the velocity waveform shape. Consequently, a velocity waveform of the same shape as the

ensemble-averaged pressure waveform was scaled to match zebra finch tidal volume data (2) and then used as the velocity boundary condition.

Model Verification

We used a model with a branching angle of $\alpha = 90°$ to verify that the results were independent of mesh density and time step size. We examined results from meshes consisting of between approximately 25,000 and 3,200,000 cells and time step sizes ranging from 10 ms to 0.05 ms (resulting in between 47 and 9,400 time steps, respectively, over a single breathing cycle), varying each independently as well as in combination.

We monitored wall shear stress at a point near the tracheobronchial juncture, a region found to have elevated wall shear stress over the course a complete breathing cycle. Grid and time step size convergence was determined by identifying parameters that resulted in grid- and time-independent wall shear stress waveforms (see Figs. S1-3 and S1-4). As wall shear stress is calculated using the velocity gradient at the wall, it is very sensitive to changes in the flow field, and therefore an excellent indicator of convergence. The results in Fig. 3a were obtained using 1,629,039 cells and a time step size of 0.5 ms.

Results

We tracked velocity and wall shear stress over two breathing cycles, with results for the second cycle shown in Fig. S1-5. During a small period when the flow is switching directions, recirculation can be seen to occur, as evidenced in the $t/T = 0/6$ time frame (where t denotes time and T denotes one period, thus t/T denotes the fraction of one breathing period).

The maximum wall shear stress during exhalation for this configuration is located near the lateral sides of the trachea near the tracheobronchial juncture, where the trachea first begins to branch out to the bronchi. The maximum wall shear stress during inhalation (and over the whole period) is observed at $t/T = 5/6$ near the pessulus (Fig. 3a; Fig. S1-5).

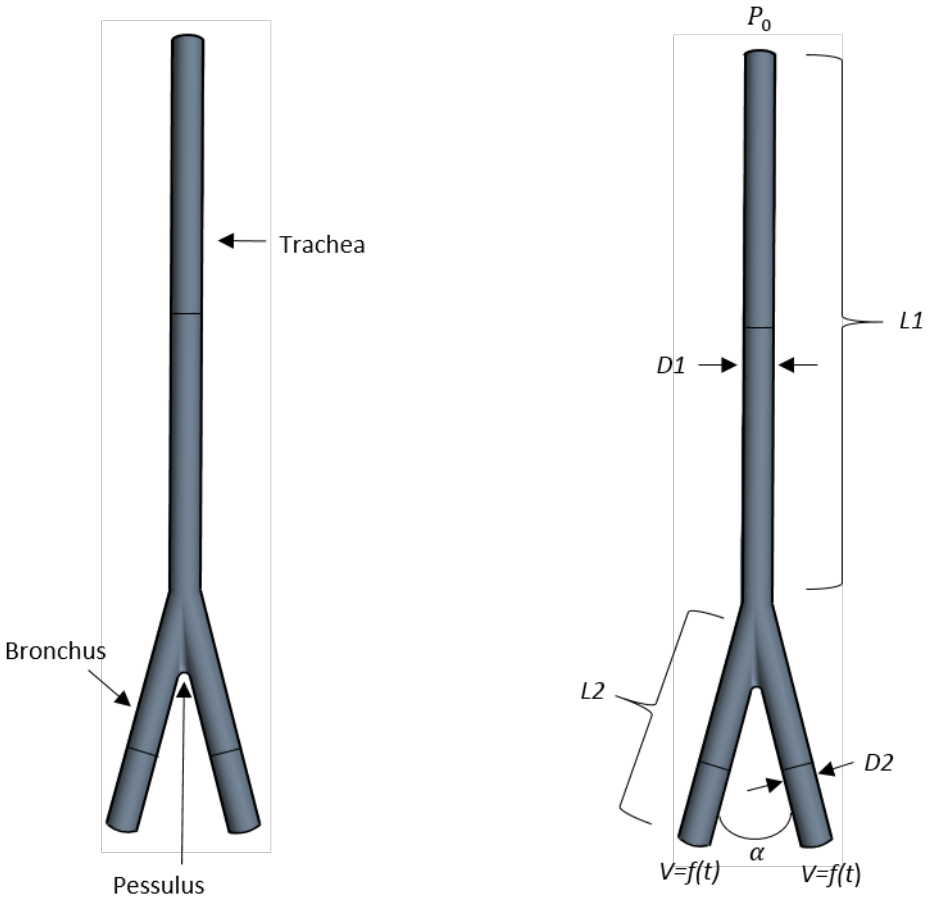

Figure S1-1: Geometric depiction of simplified parametric avian airway model. For Fig. 3a, the following values were used: D1 = 1 cm, D2 = 1 cm, L1 = 10 cm, L2 = 5 cm, and $\alpha = \boldsymbol{30}°$.

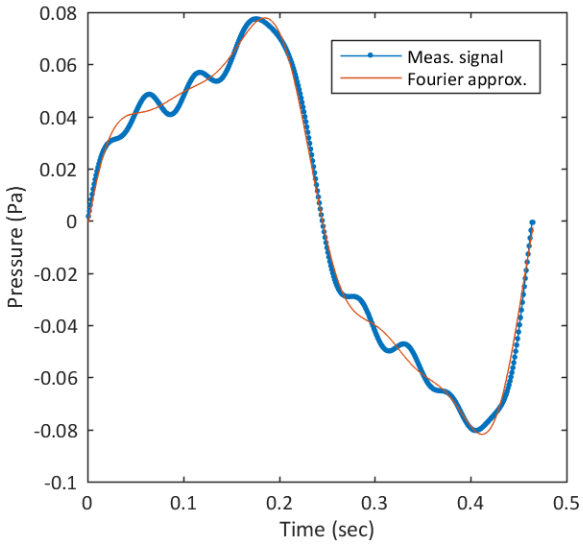

Figure S1-2: Ensemble-averaged and Fourier approximation of avian lung pressure signal from Franz and Goller (1).

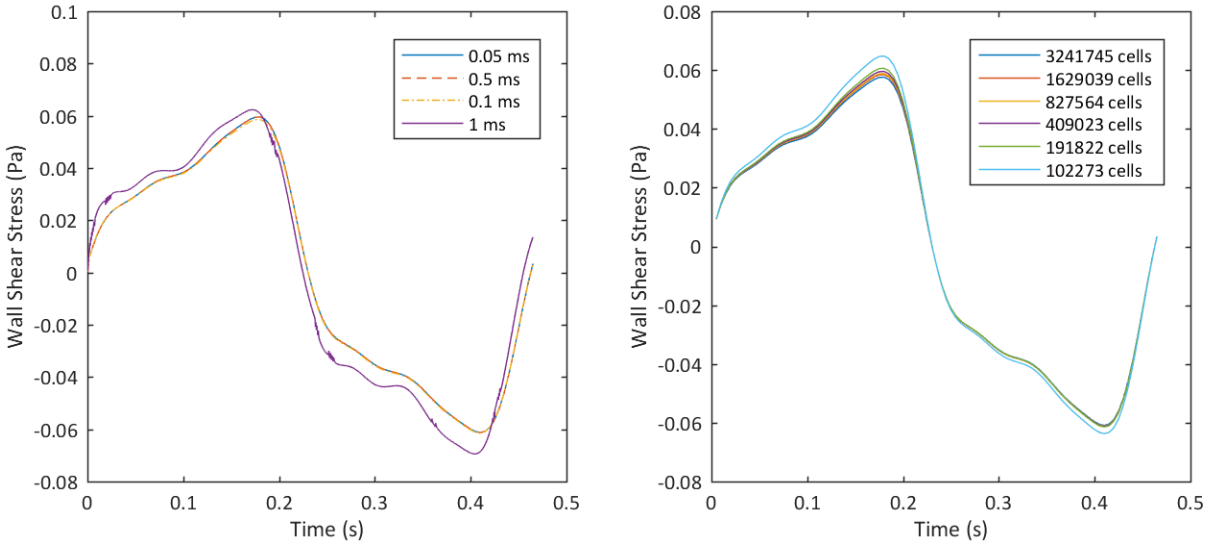

Figure S1-3: (Left): Tests to verify independence of time step size. Results from the two finest time step sizes (0.5 ms and 0.05 ms) are graphically indistinguishable, indicating convergence. (Right): Tests to verify independence of mesh size in which relatively minor variations in wall shear stress were observed.

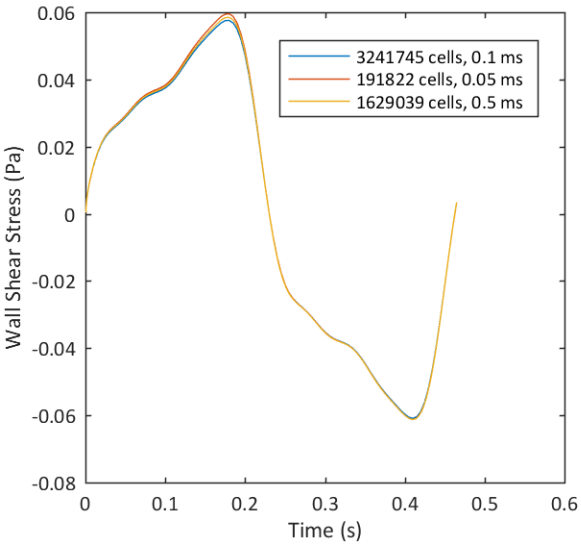

Figure S1-4: Comparison between the results from the finest grid tested, the smallest time step tested, and the final grid and time step size parameters used in the simulations shown in Fig. 3a, showing graphically-indistinguishable results and thereby demonstrating grid and time step size independence.

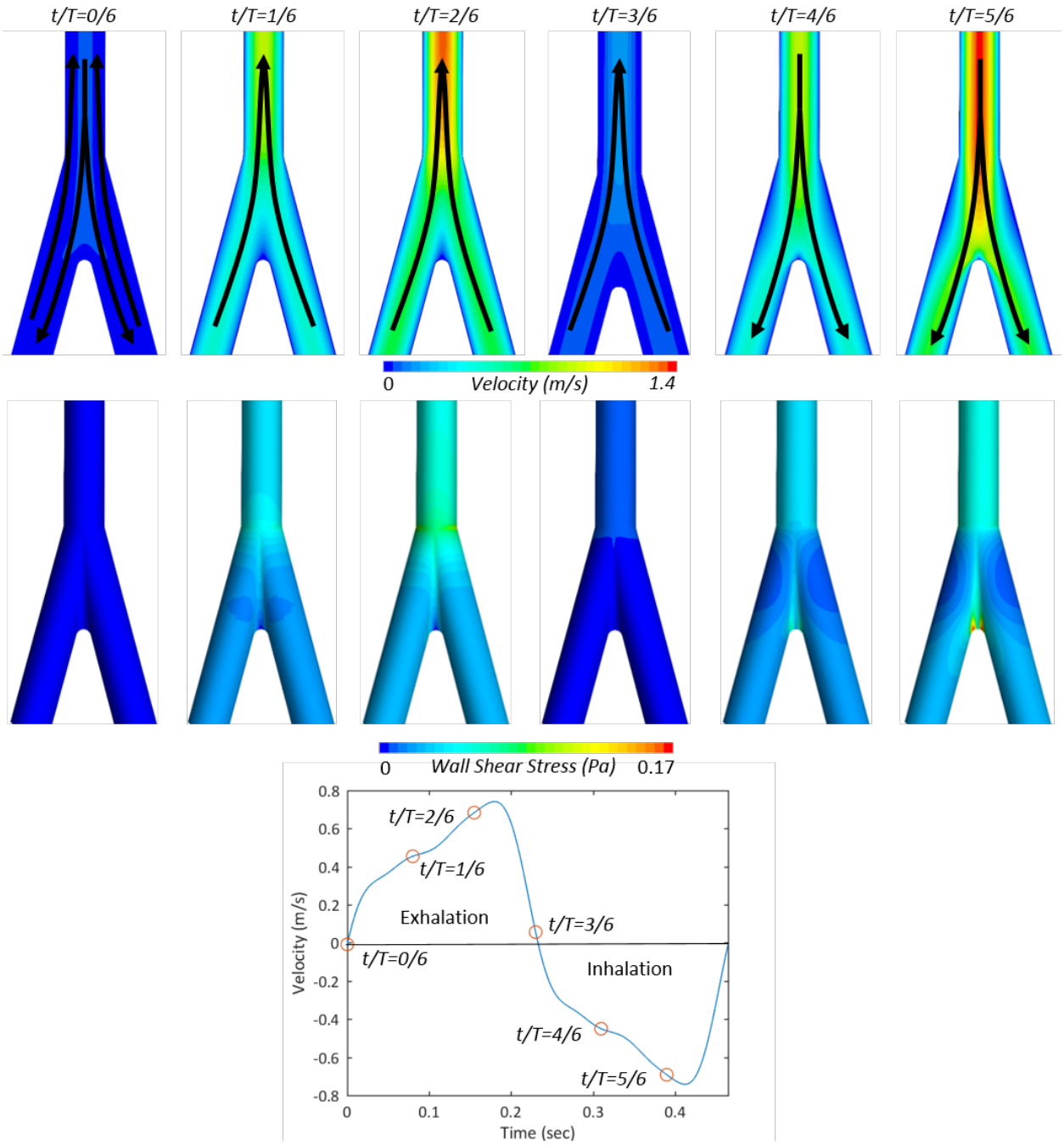

Figure S1-5: Contours of velocity (top row) and wall shear stress (bottom row) for selected phases of a breathing cycle. The phases are marked in the breathing pattern graph on the bottom, with exhalation and inhalation phases denoted. Arrows on the velocity profile plots indicate general flow direction.

Methods S2: Methods for the cartilage patterning models investigated (Fig. 3d).

We used the generalized Swift-Hohenberg equation (3) as a generic model of periodic patterning:

$$\frac{\partial \phi}{\partial t} = \quad a\phi - (\nabla^2 + L^{-2})^2\phi - c\phi^2 - \phi^3, \qquad \text{(S2-1)}$$

Here: $\phi(x)$ corresponds to the density of cartilage across the tissue; *a* controls the speed of patterning; *L* controls the spacing between the cartilage rings; and *c* is a parameter that dictates whether the pattern more closely resembles stripes or spots.

Equation S2-1 was simulated either on a rectangular domain (upper panels in Fig. 3d) or using a geometry mimicking the TBJ (lower panels in Fig. 3d). As discussed in the main text, we use the two-dimensional simulations as an approximation to the fully three-dimensional geometry of the trachea and bronchi. This approximation is accurate for surfaces in the limit of zero Gaussian curvature, which is exactly true for the cylindrical domain of the trachea, and approximately true for the TBJ. For boundary conditions, we set $\phi = 0$ everywhere outside the domain (corresponding to a situation where ϕ is rapidly degraded everywhere outside of the domain).

Simulating Equation S2-1 produces stripe-like patterns provided the parameter, *c*, is sufficiently small; however, these patterns have ill-defined orientation and do not reproduce the stereotypical circumferential orientation observed in the cartilage elements. Previous studies suggest that, in extremely thin geometries, boundary conditions can orient stripes circumferentially (for example, in the stripes on the cheetah's tail (4)). However, the measured geometry of the trachea cannot account for stripe orientation in this tissue. Instead, motivated by the exploration of pattern-orienting gradients in Hiscock and Megason (5), we modify Equation S2-1 with a spatially varying cartilage production gradient, *h*, to give:

$$\frac{\partial \phi}{\partial t} = \quad a\phi - (\nabla^2 + L^{-2})^2\phi - c\phi^2 - \phi^3 + h(x) \qquad \text{(S2-2)}$$

For simulations of the trachea, we choose $h(x)$ to vary along the length of the tube; simulations confirm that this gradient can orient stripes circumferentially. For the TBJ, we allow $h(x)$ to be a function of distance from the center of the TBJ, thereby forming a gradient not only along the length of the trachea, but also along each of the bronchi tubes, thus directing the formation of circumferential cartilage in both the trachea and the bronchi.

Simulations of Equation S2-2 for a range of parameters recapitulate several *in vivo* cartilage patterns, as shown in Fig. 3d. We find that, for small values of *a*, the patterns tend to be more regular (left); whereas, as *a* increases, stripe splitting and disorganized patterning at the TBJ emerges (right).

References:

1. **Franz M, Goller F (2002) Respiratory units of motor production and song imitation in the zebra finch. *J Neurobiol* 51(2):129–141.**

2. **Frappell PB, Hinds DS, Boggs DF (2001) Scaling of respiratory variables and the breathing pattern in birds: an allometric and phylogenetic approach. *Physiol Biochem Zool* 74(1):75–89.**

3. **Swift J, Hohenberg PC (1977) Hydrodynamic fluctuations at the convective instability. *Phys Rev A* 15(1):319–328.**

4. **Murray JD (1988) How the leopard gets its spots. *Sci Am* 258(3):80–87.**

5. **Hiscock TW, Megason SG (2015) Orientation of Turing-like Patterns by Morphogen Gradients and Tissue Anisotropies. *Cell Syst* 1(6):408–416.**